PNAS RESEARCH ARTICLE | PLANT BIOLOGY

Nanoscale regulation of ROS signaling at the plasma membrane tunes the plant response to osmotic stress

Arthur Poitout[a], José M. Ugalde[b], Lucille Gorgues[a], Armelle Dongois[a], Patricia Scholz[c], Philippe Nacry[a], Carine Alcon[a], Jean-Bernard Fiche[d], Xavier Dumont[a], Marcelo Nollman[d], Komal Jhala[e], Anton R. Schäffner[e], Yvon Jaillais[c], Lionel Verdoucq[a], Andreas J. Meyer[b], and Alexandre Martinière[a,1]

Affiliations are included on p. 10.

Edited by Alice Y. Cheung, University of Massachusetts Amherst Department of Biochemistry and Molecular Biology, Amherst, MA; received October 21, 2025; accepted April 30, 2026

The spatiotemporal organization of proteins and lipids within membranes is crucial for ensuring proper cellular signaling. While the segregation of proteins and lipids into membrane nanodomains is well established, it remains unclear whether nanodomains can generate gradients of small diffusible molecules. In plants, reactive oxygen species (ROS), especially hydrogen peroxide (H_2O_2), act as key signaling molecules in response to environmental stimuli such as osmotic stress. However, how extracellular H_2O_2 affects intracellular signaling has remained unknown. Here, we show that osmotic stimulation induces the formation of localized, H_2O_2-rich nanoenvironments at the cytoplasmic face of the plasma membrane (PM) in *Arabidopsis* root cells. Using a PM-tethered H_2O_2 biosensor, we found that these oxidized nanodomains arise from the clustering of RESPIRATORY BURST OXIDASE HOMOLOGs (RBOHs) and RHO OF PLANTS 6 (ROP6), in coordination with aquaporin-mediated H_2O_2 transport via the PLASMA MEMBRANE INTRINSIC PROTEIN2;7 (PIP2;7). These local redox hotspots at the PM create a feedforward loop in which H_2O_2 enhances ROP6 nanoclustering, thereby amplifying ROS signaling. Disruption of H_2O_2 production or transport dampens both ROP6 clustering and anisotropic cell expansion, indicating a crucial role for spatially confined redox signaling in regulating plant growth under osmotic stress. Our findings propose a model in which ROP6/RBOHD-F/PIP2;7 nanodomains function as discrete redox signaling units, redefining ROS signaling at the PM as a structured, signal-specific, and compartmentalized process.

plants | reactive oxygen species | Rho GTPase | osmotic signal | aquaporin

Significance

Cellular membranes are not mere barriers but active platforms that regulate signaling specificity. Here, we uncover how plant cells use nanoscale membrane organization to shape localized H_2O_2 concentration during osmotic stress. Using a genetically encoded H_2O_2 biosensor targeted to ROP6 nanodomains, we reveal the formation of oxidized nanoenvironments at the plasma membrane. These domains depend on coordinated activity between NADPH oxidases RBOHs and aquaporin PIP2;7, which enables H_2O_2 diffusion across the membrane. Importantly, localized H_2O_2 reinforces ROP6 clustering, establishing a feedforward loop that enhances ROS production and supports cell growth under stress. This study highlights how spatial coupling of protein clusters with redox gradients enables plants to achieve signal specificity, offering a model for membrane-confined ROS signaling.

The plasma membrane (PM) is a dynamic mosaic of lipids and proteins organized into heterogeneous patches of distinct size, composition, and function, commonly referred to as nanodomains (1–3). These nanodomains are recognized as platforms modulating protein–protein and protein–lipid interactions, thereby playing central roles in the spatial and temporal regulation of signaling pathways. As such, biological membranes are not passive barriers but active participants in signal integration (1). A major challenge in cell biology is to elucidate how membrane organization and dynamics quantitatively influence core features of signaling such as specificity, processing, and amplification, ultimately shaping cellular responses.

In plants, the production of reactive oxygen species (ROS) triggers a broad set of molecular responses to environmental stimuli as well as key developmental processes. In many cases, ROS generation is initiated in the extracellular matrix (the apoplast) where superoxide ($O_2^{\cdot-}$) is produced by NADPH oxidases, known as RESPIRATORY BURST OXIDASE HOMOLOGs (RBOHs) in plants (4–6). Superoxide is rapidly converted into hydrogen peroxide (H_2O_2), which serves as a more stable signaling molecule.

Apoplastic H_2O_2 can be directly perceived by PM-localized receptor-like kinases such as HYDROGEN-PEROXIDE-INDUCED Ca^{2+} INCREASES 1 (HPCA1), which triggers cytosolic Ca^{2+} influx and contributes to the propagation of systemic ROS waves for long-distance signaling (7–9). In parallel, a fraction of apoplastic H_2O_2 diffuses across the PM and reaches the cytosol, where it can oxidize thiol groups to sulfenic acid. These intermediates may further react to form mixed disulfides with glutathione or other proteins, or form intramolecular disulfide bonds (10, 11). Such posttranslational modifications (PTMs) often modulate the localization, conformation, or activity of target proteins (12–14).

Despite advances in our understanding of the perception and integration of ROS signals, the spatial regulation of H_2O_2-dependent signaling has remained poorly understood.

The authors declare no competing interest.

This article is a PNAS Direct Submission.

[1]To whom correspondence may be addressed. Email: alexandre.martiniere@cnrs.fr.

This article contains supporting information online at https://www.pnas.org/lookup/suppl/doi:10.1073/pnas.2529740123/-/DCSupplemental.

Published June 22, 2026.

For instance, it remains unclear whether elevated H_2O_2 levels are uniform throughout the cell or whether variations in H_2O_2 levels exist between subcellular regions during signaling events. Addressing this gap is key to understand the specificity and dynamics of ROS-mediated signaling.

Rho of Plants (ROPs) form a plant-specific clade of small GTPases that play essential roles in regulating polarized cell growth, such as in root hairs and pollen tubes (15–17). Like other Rho-family GTPases, ROPs function as molecular switches that cycle between an inactive GDP-bound form and an active GTP-bound state. In their active conformation, ROPs interact with a range of effector proteins to modulate diverse downstream cellular processes (15). Notably, direct physical interactions between GTP-bound ROPs and RBOHs have been demonstrated through both biochemical and structural approaches (18–22). These interactions suggest a mechanistic link between ROP activation and ROS production. Genetic evidence further supports this connection, given that overexpression of constitutively active (CA) ROPs leads to elevated ROS levels, while ROP loss-of-function mutants exhibit impaired ROS accumulation (23–26). Together, these findings suggest that ROPs are positive regulators of RBOH-mediated ROS production, integrating membrane-localized signaling cues with redox-based cellular responses.

Previous studies have shown that ROP6 bind to the PM in root epidermal cells via prenylation of its C-terminus (25, 27). Using single-molecule localization microscopy, it was shown that within minutes of hyperosmotic stimulation, a subset of mEOS2-ROP6 molecules reorganizes into nanodomains of approximately 50 nm in diameter within the PM (21, 28). These ROP6 nanodomains are critical signaling hubs, required for the ROS increase in response to osmotic stress. Importantly, osmotic stimulation leads to the colocalization of ROP6 with RBOHD and RBOHF within the nanodomains. This suggests that osmotic cues trigger the activation and spatial reorganization of ROP6, promoting its clustering with RBOHD/F to initiate ROS production. However, while these observations strongly support a role for ROP6/RBOH nanodomains in ROS signaling, it remains unresolved if these clusters constitute a functional and spatially regulated signaling unit that integrates ROS production with signal specificity at the PM during osmotic stress.

Using the genetically encoded H_2O_2–sensitive biosensor HyPer7 (29, 30), this study reveals that osmotic stimulation induces the formation of H_2O_2-enriched nanoenvironments on the cytoplasmic side of the PM. These oxidized nanodomains arise from the localized activity of RBOHs and a facilitated H_2O_2 diffusion, specifically within ROP6-containing nanodomains. Surprisingly, the spatially restricted oxidation at the nanodomains creates a feedforward loop, in which the local increase of H_2O_2 levels further promotes ROP6 clustering. This, in turn, amplifies ROS production and contributes to cellular growth under osmotic stress.

Results

HyPer7-ROP6HyPer7 Allows Detection of Osmotically Induced ROS in *Arabidopsis* Root Cells. To monitor osmotically induced H_2O_2 accumulation near its production site, we generated a fusion construct between HyPer7, a highly sensitive hydrogen peroxide (H_2O_2) ratiometric sensor (29, 30) and ROP6 that interacts with the NADPH oxidase RBOHD/F after osmotic stimulation (18–22) (Fig. 1*A*). The HyPer7 protein was fused to the N terminus of ROP6 to avoid interfering with its function (21, 27, 31). As expected, the HyPer7-ROP6 signal in *Arabidopsis* root tip cells localized predominantly at the PM, with only minimal cytosolic labeling, compared to the diffuse distribution observed with soluble HyPer7 (Fig. 1*B*). To assess the fluorescent properties of HyPer7-ROP6 *in planta*, we treated seedlings with increasing concentrations of H_2O_2 and compared their responses to plants expressing soluble HyPer7. The response curves of both lines were similar, indicating that the ROP6 fusion does not compromise the dynamic range of the HyPer7 sensor (*SI Appendix*, Fig. S1*A*). Furthermore, plants expressing either HyPer7 or HyPer7-ROP6 displayed no significant growth defects compared to the Col-0 wild type (*SI Appendix*, Fig. S1*B*).

Based on these results, we selected the HyPer7-ROP6 line for a detailed characterization of H_2O_2 signaling in response to osmotic stress. Five-day-old seedlings expressing HyPer7-ROP6 were transiently exposed to a hyperosmotic solution (−0.75 MPa) by perfusion. Since HyPer7 has an increased fluorescence excitation peak at 488 nm when oxidized, and at 405 nm when reduced, we generated an Ex488/Ex405 ratio image to record its relative oxidation level. Within seconds of osmotic stimulus application, we observed a sharp increase in the Ex488/Ex405 ratio, followed by a plateau reached after 5 min (Fig. 1 *C* and *D* and *SI Appendix*, Fig. S1*C*). In contrast, washing out the hyperosmotic solution led to a decrease in the ratio, returning close to baseline levels (Fig. 1 *C* and *D* and *SI Appendix*, Fig. S1*C*). Perfusion with a control buffer resulted only in a slight but nonsignificant increase in the ratio (Fig. 1*C* and *SI Appendix*, Fig. S1*C*). These findings indicate that osmotic stimulation leads to a significant and reversible increase in cytoplasmic oxidation. These findings show that osmotic stimulation leads to a pronounced and reversible increase in cytoplasmic oxidation revealed by the HyPer7-ROP6 probe. Taken together, our results demonstrate that HyPer7 is effective for detecting osmotic stress-induced alterations of cytosolic H_2O_2 levels, and that targeting of HyPer7 to the PM as a ROP6 fusion does not compromise its oxidation sensitivity nor induce any observable phenotypic changes *in planta*.

Osmotic Stimulation Induces Oxidized Nanoenvironments at the PM. Since osmotic signaling induces the clustering and interaction of ROS-producing enzymes RBOHD and RBOHF with ROP6 (21), we hypothesized that this could lead to localized HyPer7 oxidation. Given that ROP6 nanodomains are clearly visible under Total Internal Reflection Fluorescence (TIRF) microscopy, we developed a method to quantify the degree of sensor oxidation under TIRF illumination (see *Materials and Methods* section). Under control condition, HyPer7-ROP6 displayed a uniform signal at the PM when excited at both 405 nm and 488 nm. We then generated ratio images between the sequentially imaged channels 488 nm/405 nm and calculated a mean ratio value of 1.8 ± 0.24 (Fig. 1 *E* and *G* and *SI Appendix*, Fig. S1 *D* and *E*). To validate our method, we applied increasing concentrations of exogenous hydrogen peroxide (H_2O_2), which resulted in a stepwise increase of the ratio values, consistent with dose-dependent oxidation of HyPer7-ROP6 (*SI Appendix*, Fig. S1 *D* and *E*). These results demonstrate that ratiometric TIRF microscopy enables reliable monitoring of the oxidation dynamics of the HyPer7-ROP6 sensor at the PM of living plant cells.

After 15 min of osmotic stimulation, a portion of the HyPer7-ROP6 signal was found to accumulate in discrete clusters at the PM (Fig. 1*E*). These clustering patterns closely mirror previous results obtained using GFP-ROP6 expressing lines (21, 28, 32), indicating that the HyPer7 fusion does not interfere with osmotic-induced ROP6 clustering. Interestingly, the ratio images revealed that the 488 nm/405 nm ratio values within these ROP6 nanodomains were significantly higher than those in adjacent membrane

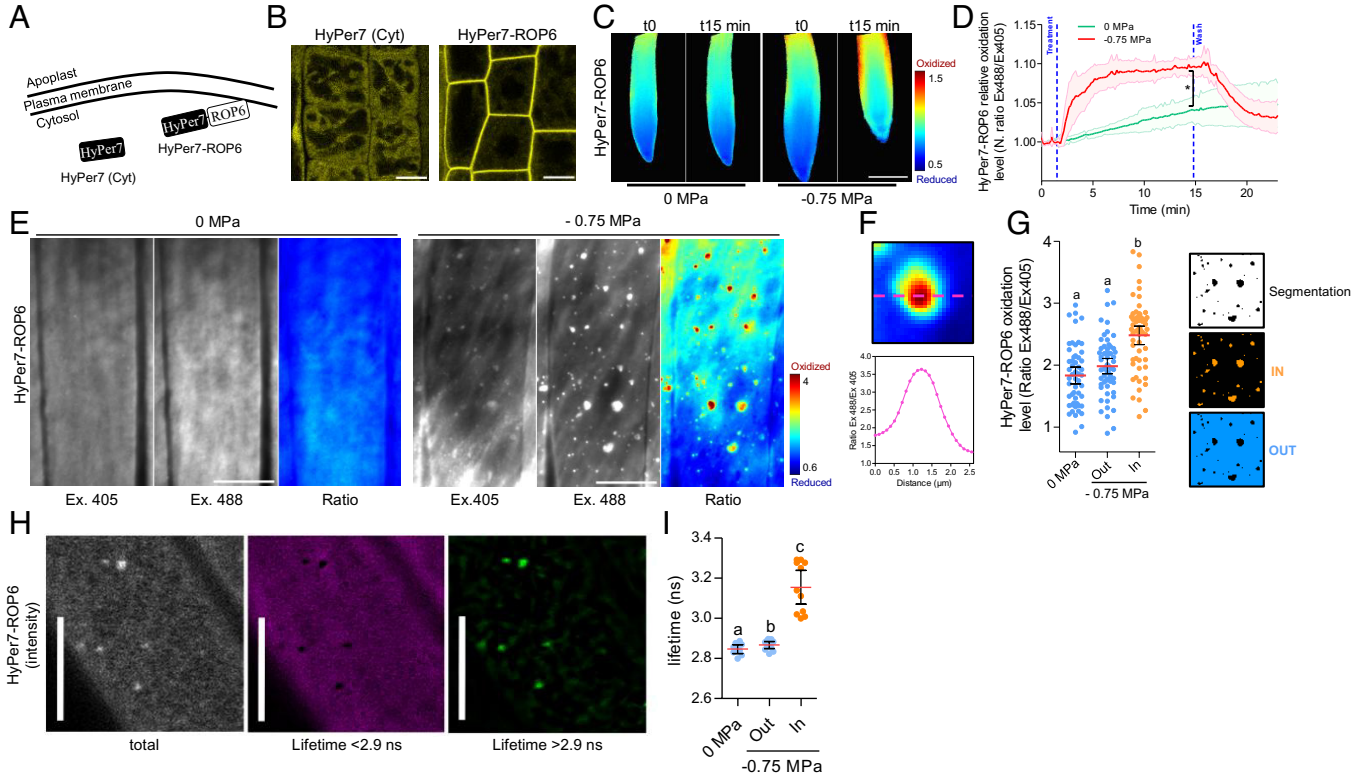

Fig. 1. HyPer7-ROP6 reveals formation of ROS nanoenvironments at the PM in response to osmotic shock. (*A*) Scheme of the cellular localization of HyPer7 sensor in its free form or fused to ROP6. (*B*) Confocal images of epidermal root tip cells expressing HyPer7 or HyPer7-ROP6. (*C*) Ratiometric images of 5-day-old *Arabidopsis* plants expressing HyPer7-ROP6 in control condition (0 MPa) or upon osmotic stimulation (−0.75 MPa). (*D*) Typical time course showing HyPer7-ROP6 oxidation level (N. Ratio Ex488/Ex405) in response to control (0 MPa) or hyperosmotic stimulation (−0.75 MPa). All ratios are normalized to the mean value from t = 0 to 2 min. (*E*) Intensity-based (Ex405 and Ex488) and ratio-based (Ratio) TIRF images of HyPer7-ROP6-expressing root epidermal cells in control condition (0 MPa) or after 15 min osmotic stimulation (−0.75 MPa). (*F*) Zoom-in of a HyPer7-ROP6 nanodomain and its ratio (Ex488/Ex405) along the dashed line. (*G*) Quantification of HyPer7-ROP6 oxidation level in control condition (0 MPa) or upon osmotic stimulation (−0.75 MPa) where signal inside or outside HyPer7-ROP6 nanodomains was segmented as illustrated aside the graph. (*H*) Image segmentation based on lifetime values < or > than 2.9 ns, of a cell expressing Hyper7-ROP6 under osmotic stimulation. (*I*) Quantification of HyPer7-ROP6 lifetime value in control condition (0 MPa) or upon osmotic stimulation (15 min at −0.75 MPa) inside and outside osmotically induced ROP6 nanodomains. Mean with error bars correspond to the 95% CI. For D * *t* test, *P* value < 0.05 at t = 15 min. n is at least five seedlings from three independent replicates. For *G* and *I*, letters show significant differences according to a one-way ANOVA and Tukey's multiple comparisons test at $P < 0.05$. For *G*, n cells are >53 from >9 seedlings from three independent replicates. For *I*, n cells are >9 from six seedlings from two independent replicates. For *B*, the scale bar is 20 µm; for *C*, the scale bar is 50 µm; and for *E* and *H*, the scale bar is 10 µm.

regions where HyPer7-ROP6 is also present (Fig. 1 *E* and *F*). To quantify this difference, we performed an image segmentation to separate fluorescence located in HyPer7-ROP6-enriched nanodomains (Fig. 1*G*, orange) from fluorescence outside these nanodomains (Fig. 1*G*, blue). In osmotically treated cells, HyPer7-ROP6 ratio values were consistently elevated within nanodomains, while values outside these domains remained similar to those observed in untreated control cells (prior to any osmotic stimulation). This indicates that HyPer7 oxidation is spatially restricted and occurs specifically within nanodomains where ROP6 accumulates (Fig. 1*G*).

To eliminate the possibility of changes in HyPer7 concentration affecting its photophysical properties and complicating our interpretation, we produced recombinant HyPer7 protein. Varying the protein concentration by more than twofold did not result in significant changes in the fluorescence ratio, confirming that the ratiometric signal from the sensor is not substantially influenced by its concentration (*SI Appendix*, Fig. S1*F*).

To further validate our findings, we measured HyPer7 fluorescence lifetime, which is less affected by sensor concentration than intensity. It remains responsive to oxidative changes as fluorescence lifetime increases in a dose-dependent manner to exogenous application of H_2O_2 (*SI Appendix*, Fig. S1*G*). Minutes after osmotic stimulation, cells expressing HyPer7-ROP6 displayed an increased fluorescence lifetime, consistent with sensor oxidation (*SI Appendix*, Fig. S1*H*). Notably, pixel-wise lifetime segmentation revealed that elevated lifetimes were specifically confined to plasma membrane nanodomains (Fig. 1 *H* and *I*). These results indicate that osmotic changes induce a localized ROS accumulation restricted to ROP6-containing nanodomains, revealing the presence of spatially confined H_2O_2-rich nano environments at the cytoplasmic face of the PM.

To investigate whether this local H_2O_2 accumulation propagates deeper into the cytoplasm, we examined HyPer7 expressing lines under ratio-TIRF. Upon osmotic stimulation, no significant changes in mean HyPer7 ratio values nor distinct subcellular patterns were observed (*SI Appendix*, Fig. S2 *A* and *B*). These observations suggest that the oxidized nano environments detected near the PM using HyPer7-ROP6 does not extend into the broader cytosolic space, supporting the existence of spatially restricted H_2O_2 close to the cell surface. Given that our observations suggest H_2O_2 accumulation originates from discrete, nanodomains at the PM, we next investigated how this is modulated by the intensity of the osmotic stimulus. To this end, we applied a milder osmotic treatment (–0.26 MPa) to plants expressing HyPer7-ROP6. Compared to the stronger stimulus (–0.75 MPa), the mild treatment resulted in a noticeable shift toward lower ratio values in ROP6 nanodomains (*SI Appendix*, Fig. S2 *C* and *D*). These data

suggest a direct correlation between the osmotic stress intensity and nanodomain oxidation level.

To further examine the dynamic relationship between an osmotic signal and localized oxidation, we performed washout experiments. Fifteen minutes after removal of the osmotic stimulus, HyPer7-ROP6 ratio values in nanodomains decrease significantly (*SI Appendix*, Fig. S2 *E* and *F*). These trends became even more pronounced 1 h after washout, indicating a full reversibility of nanodomain redox status in response to osmotic cues, even if ROP6 containing nanodomains are still present. Taken together, these results demonstrate that the strength of osmotic stimulation quantitatively correlates with the oxidation level below ROP6 nanodomains at the PM.

The Formation of Oxidized Nanoenvironments at the PM Is Signal Specific. We next asked whether the formation of osmotically induced oxidized nanoenvironments reflects signal-specific cellular responses. To test this hypothesis, we examined the auxin signaling pathway, which also involves ROP6 clustering in both root and leaf epidermal cells (27, 31). Similar to GFP-ROP6, auxin treatment induced the formation of HyPer7-ROP6 nanodomains in root epidermal cells (Fig. 2*A*). However, the HyPer7-ROP6 ratio values within these auxin-induced nanodomains did not differ significantly from those in surrounding membrane regions (Fig. 2*B*). This finding was further confirmed at the tissue level, where auxin stimulation did not elicit any detectable changes in overall HyPer7-ROP6 oxidation (Fig. 2 *C* and *D*). These results

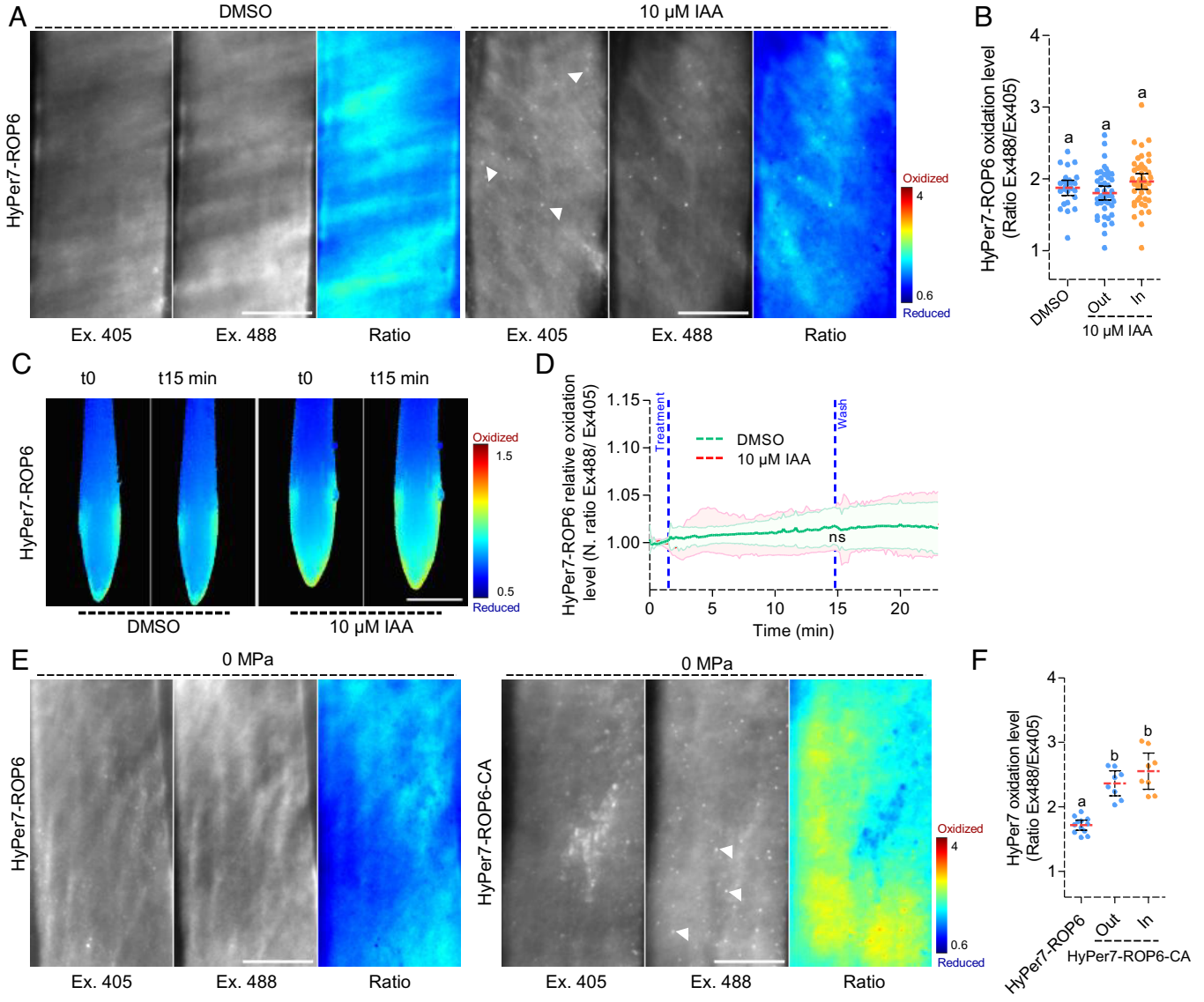

Fig. 2. Local HyPer7-ROP6 oxidation is not observed after auxin stimulation. (*A*) Intensity-based (Ex405 and Ex488) and ratio-based (Ratio) TIRF images of HyPer7-ROP6–expressing root epidermal cells in control (DMSO) or after 10 μM auxin (IAA) stimulation for 30 min. (*B*) Comparison of HyPer7-ROP6 ratio values in control (DMSO) or after 10 μM auxin (IAA) stimulation inside or outside HyPer7-ROP6 nanodomains. (*C*) Ratiometric images of 5-day-old *Arabidopsis* plants expressing HyPer7-ROP6 in control condition or upon 10 μM auxin stimulation. (*D*) Typical time course showing HyPer7-ROP6 oxidation level (N. Ratio Ex488/Ex405) in response to control (DMSO) or after 10 μM auxin (IAA) stimulation. All ratios are normalized to the mean value from t = 0 to 2 min. (*E*) Intensity-based (Ex405 and Ex488) and ratio-based (Ratio) TIRF images of HyPer7-ROP6 and HyPer7-ROP6-CA-expressing root epidermal cells in control condition. (*F*) Quantification of HyPer7-ROP6-CA ratio values in control condition either inside or outside HyPer7-ROP6-CA nanodomains. Mean with error bars correspond to the 95% CI. For *B* and *F* letters show significant differences according to a one-way ANOVA and Tukey's multiple comparisons test at $P < 0.05$. For B, n >25 cells from >9 seedlings from three independent replicates. For *F*, n >8 cells from >4 seedlings from two independent replicates. For *D*, *t* test, *P*-value = 0.5058, n.s. means no significant differences n >5 seedlings from three independent replicates. (*A* and *E*, Scale bar 10 μm. *C*, Scale bar 50 μm.)

suggest that the formation of oxidized nanoenvironments at the PM is specific to osmotic stress and does not arise from ROP6 clustering alone. Instead, it likely depends on the coclustering of ROP6 with the ROS-producing enzymes RBOHD and RBOHF that only happens after osmotic stimulation and not auxin (21).

We then investigated to what extent ROP6 activation alone is sufficient to induce oxidized nanoenvironments at the PM. The expression of a constitutively active ROP6 variant carrying the G15V point mutation (ROP6-CA), which keeps the protein in its GTP-bound form, is known to promote ROP6 clustering and its interaction with RBOHD, even in the absence of external stimuli (21, 27, 31). As a result, ROP6-CA expression leads to basal H_2O_2 accumulation in plant cells (23–26, 33). Consistent with previous findings with GFP-ROP6-CA, HyPer7-ROP6-CA expressing lines exhibited small size nanodomains at the PM under nonstimulated conditions (Fig. 2*E*). In this case, however, HyPer7-ROP6-CA ratio values were elevated both within and outside of nanodomains in ROP6-CA-expressing cells compared to control HyPer7-ROP6 lines (Fig. 2*F*). These results indicate that constitutively active ROP6 is sufficient to induce both membrane clustering and HyPer7-ROP6-CA oxidation. However, the absence of spatially confined oxidation (i.e., similar ratio values inside and outside nanodomains) and the limited size of ROP6-CA nanodomains suggest that ROP6 activation alone does not recreate the condition in which the oxidized nanoenvironments are observed in response to osmotic stress. This implies that additional regulatory mechanisms are required to spatially restrict ROS production at the PM.

H_2O_2 Transport across the PM via Aquaporin Is Necessary for Establishing Osmotically Induced Oxidized Nanoenvironments. Based on our results, we conclude that osmotic stimulation triggers the formation of oxidized nanoenvironments on the cytoplasmic side of the PM. However, it is well established that RBOH enzymatic activity consumes cytoplasmic NADPH to produce O_2^- in the extracellular space i.e., the apoplast. Given the short lifetime of O_2^- (in the order of milliseconds), O_2^- is generally assumed to be rapidly converted to H_2O_2 via dismutation and/or the action of superoxide dismutases (34, 35). Therefore, to explain the increased oxidation in the cytoplasm, we hypothesize the existence of a molecular mechanism that facilitates the translocation of an oxidizing agent, most likely H_2O_2, across the plasma membrane.

To test this hypothesis, we treated HyPer7-ROP6-expressing plants with catalase, a membrane-impermeable H_2O_2 scavenger, and then applied an osmotic stimulus. Catalase treatment did not abolish ROP6 nanodomain formation but markedly reduced HyPer7 oxidation in HyPer7-ROP6 nanodomains (Fig. 3 *A*, *B*, and *F*). These findings support a model in which RBOH-mediated O_2^- production results in higher H_2O_2 levels in the apoplast, which must then cross the PM to oxidize HyPer7 in the cytoplasm. Conversely, coapplication of exogenous H_2O_2 with osmotic stimulation enhanced oxidation levels of HyPer7-ROP6 nanodomains (Fig. 3 *A*, *B*, and *F*). In addition, we observed that catalase treatment and exogenous H_2O_2 application have opposite effects on ROP6 nanodomain size and, to a lesser extent, on their density (Fig. 3*G* and *SI Appendix*, Fig. S4*D*). These observations suggest an interplay between cytoplasmic H_2O_2 accumulation and ROP6 nanodomains' sizes and number.

Interestingly, exogenous H_2O_2 in the absence of any osmotic stimulation failed to generate oxidized nanoenvironment (*SI Appendix*, Fig. S1*D*). This suggests that osmotic signaling is required to enable or facilitate H_2O_2 diffusion through ROP6-containing nanodomains, reinforcing the idea that ROS signaling at the membrane is highly regulated and context-dependent.

To better understand the mechanism by which H_2O_2 might be diffusing from the apoplast to the cytoplasm within osmotically induced nanodomains, we explored the involvement of aquaporins. Indeed, aquaporins are membrane channel proteins primarily known for facilitating water transport, but certain isoforms such as *Arabidopsis* PIP2;1; PIP2;2, PIP2;4, PIP2;5, PIP2;6, and PIP2;7 have also been shown to mediate the diffusion of H_2O_2 across membranes in various assays (36–38). The Plasma Membrane Intrinsic Protein 2 (PIP2) subfamily comprises a set of eight, highly homologous isoforms (39, 40), which have also overlapping functions. To overcome this, we generated a higher-order aquaporin mutant line from available single knockout lines, *5xpip2* (*pip2;1-1xpip2;2-3 pip2;4-1xpip2;6-3xpip2;7-4*), in which all the PIP2 isoforms that are highly expressed in the roots are knocked out (*SI Appendix*, Fig. S3 *A*, *D*, and *E*) (41, 42). We introduced HyPer7-ROP6 construct into this background to assess the impact of PIP2s into osmotic stress-triggered ROS signaling. First, we exposed Col-0 and *5xpip2*xHyPer7-ROP6 expressing plants to 10 mM H_2O_2 to fully oxidize the sensor. The apparent dynamic range of HyPer7-ROP6 for the ratio change between steady state and full oxidation after treatment of seedlings with 10 mM H_2O_2 was found similar in both backgrounds (*SI Appendix*, Fig. S4*A*), confirming that the sensor's performances are not affected. We tested if H_2O_2 membrane permeability is affected in *5xpip2.* HyPer7-ROP6-expressing roots in the *5xpip2* background exhibited a slower oxidation response following exposure to 100 µM exogenous H_2O_2 ($K_{Col\text{-}0} = 0.0255.s^{-1} \pm 0.0067$; $K_{5xpip2} = 0.0116.s^{-1} \pm 0.0082$) (*SI Appendix*, Fig. S4*B*). These results indicate that *5xpip2* mutants display reduced H_2O_2 permeability across the PM.

Under TIRF microscopy, HyPer7-ROP6 nanodomains in the *5xpip2* background were still able to form after osmotic stimulation but appear smaller and exhibited lower oxidation levels compared to Col-0 (Fig. 3 *D*, *H*, and *I*). Interestingly, this effect was not as strong as after catalase treatment, suggesting that some H_2O_2 can still diffuse across the membrane and consequently that ROS-producing enzymes are still functional in *5xpip2.* To test this hypothesis more directly, we used dehydroethidium (DHE), a cell permeant dye that is primarily sensitive to O_2^- in vitro and that labels the ROS including in the apoplast (43). Following osmotic treatment, both Col-0 and *5xpip2* roots showed comparable levels of DHE oxidation (Fig. 3*J*), suggesting that RBOH activity remains intact in the *5xpip2* background. Together, these results demonstrate that both pharmacological (catalase) and genetic (*5xpip2*) disruptions of H_2O_2 diffusion from the apoplast to the cytoplasm significantly impact the oxidation status of osmotically induced nanoenvironments at the PM. This supports the idea that the movement of H_2O_2 across the membrane is a critical regulatory step in the localized signaling of ROS after osmotic signal.

To address whether the contribution of PIP2 aquaporins to osmotic signaling arises from the additive effects of multiple isoforms or is driven by specific individual PIP2 proteins, we generated a *pip2* triple mutant line from single knockout lines 3x*pip2* (*pip2;1-2xpip2;2-3xpip2;4-1*) expressing HyPer7-ROP6 after genetic transformation (*SI Appendix*, Fig. S3 *B* and *E*). Upon osmotic stimulation, *3xpip2*xHyper7-ROP6 show no difference in ROP6 nanodomain oxidation compared to control lines (Fig. 3*H* and *SI Appendix*, Fig. S4*C*). Whereas ROP6 nanodomain density is reduced in *3xpip2*xHyper7-ROP6, their size remains unchanged compared to control plants (Figs. 3*I* and 4*E*). This result suggests that PIP2;1, PIP2;2 and PIP2;4 have a minor role in the formation of local ROS nano environments in root epidermal cells. PIP2;7 was previously shown to be abundant in root cells (41). In addition, mVenus-PIP2;7 expressed under the control of its endogenous promoter localizes at the PM of epidermal root tip cells like mCitrine-ROP6 does (44) (*SI Appendix*, Fig. S4*H*). Therefore, we crossed *pip2;7-2*, a

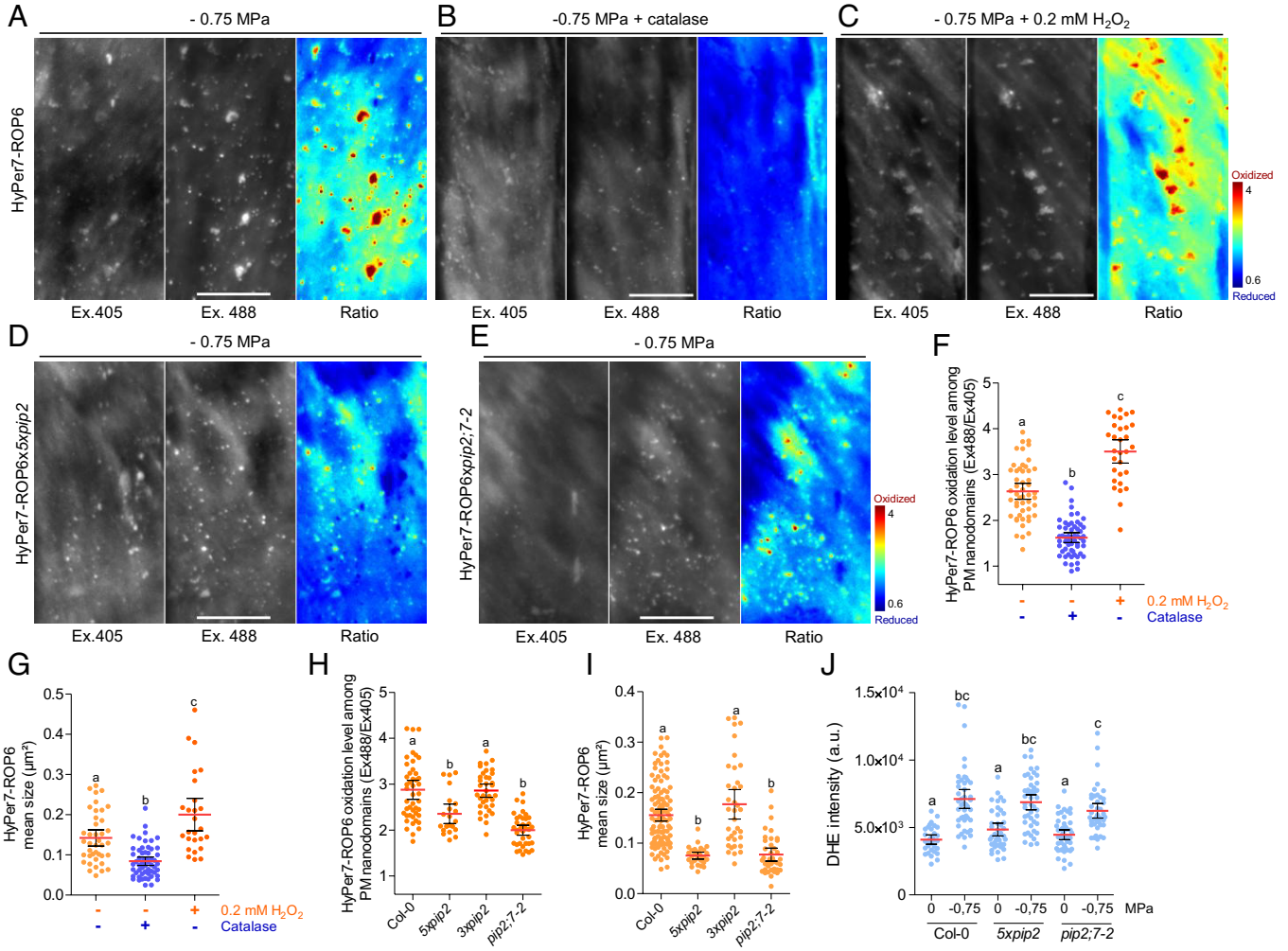

Fig. 3. Aquaporins are necessary for the establishment of osmotically induced H_2O_2 nanoenvironments. (*A–C*) Intensity-based (Ex405 and Ex488) or ratio-based (Ratio) TIRF images of HyPer7-ROP6-expressing root epidermal cells upon strong osmotic stimulation (−0.75 MPa for 15 min) cotreated with catalase, *B* or H_2O_2 (0.2 mM) *C*. (*D* and *E*) Intensity-based (Ex405 and Ex488) or ratio-based (Ratio) TIRF images of HyPer7-ROP6-expressing root epidermal cells upon osmotic stimulation (−0.75 MPa for 15 min) in *5xpip2*, *D* or *pip2;7-2*, *E*. (*F*) Quantification of nanodomains mean ratio values after osmotic stimulation (15 min, −0.75 MPa) cotreated with catalase, or H_2O_2 (0.2 mM) and of their respective mean size in *G*. (*H*) Quantification of nanodomains mean ratio values after osmotic stimulation (15 min, −0.75 MPa) in Col-0, *5xpip2*, *3xpip2,* and *pip2;7-2* backgrounds and of their respective mean size in *I*. (*J*) Dehydroethidium fluorescence quantification in Col-0, *5xpip2,* and *pip2;7-2* backgrounds in control condition or after 15 min strong (−0.75 MPa) osmotic stimulation. Mean with error bars correspond to the 95% CI. For *F–J*, letters show significant differences according to a one-way ANOVA and Tukey's multiple comparisons test at $P < 0.05$. For *F* and *G*, n > 30 cells from >9 seedlings from three independent replicates. For *H* and *I*, n cells > 21 from 10 seedlings from three independent replicates. For *J*, n cells > 31 from 10 seedlings from three independent replicates. The scale bar is 10 µm.

pip2;7 allele independent from *pip2;7-4* included in *5xpip2* to generate *pip2;7-2*xHyPer7-ROP6 line (*SI Appendix*, Fig. S3 *C–E*). We found that in response to an osmotic stimulation, although roots showed comparable levels of DHE oxidation to Col-0 (Fig. 3*J*), HyPer7-ROP6 nanodomains were less oxidized, which closely resembled the phenotype observed in the *5xpip2* mutant line (Fig. 3 *A*, *D*, *E*, and *H*). One more time, this is also correlated with a reduction in HyPer7-ROP6 nanodomains in *pip2;7-2* (Fig. 3 *A*, *D*, *E*, and *I*). To explore whether these differences might arise from a delayed ROS response in the aquaporin mutant, we quantified ROP6 nanodomain sizes and oxidation ratios after longer treatment times. For neither of these parameters, oxidation ratios nor nanodomain sizes, we observed an increase in *pip2;7-2* (*SI Appendix*, Fig. S4 *F* and *G*). These results suggest that the defects observed in aquaporin loss-of-function lines are not due to delayed responses.

All together, these results indicate that PIP2;7 is a major *PIP2* isoform that facilitates H_2O_2 diffusion across the PM, leading to the formation of H_2O_2 nanoenvironments in the cell epidermis. Thus, the *pip2;7* mutant provides a unique opportunity to test the functional importance of the localized H_2O_2 nanoenvironments for plant responses to an osmotic signal.

At the cellular level, osmotic signal trigger pronounced anisotropic cell expansion in root elongation zone after several hours of treatment (45, 46). Even if it is not fully understood yet, the loss of cell isotropic growth is the result of cell wall weakening during osmotic readjustment. This response is partially regulated by ROP6 (21). Consistent with this, we found that the double mutant of ROS-producing enzymes, *rbohd/f*, displays an impaired cell swelling response similar to that observed in *rop6-2* plants (Fig. 4 *A* and *B*). We next tested this response in aquaporin mutants, in which the ROS levels are increased after osmotic stress in the apoplast but not in the cell cortex. Both the *5xpip2* and *pip2;7-2* mutants showed reduced cell swelling responses compared to the wild type. By contrast, the *3xpip2* mutant, which did not impact the formation of oxidized nanodomains, showed a cell swelling similar to the wild type, suggesting that the H_2O_2-oxidized nanoenvironment positively regulates anisotropic cell growth in response to osmotic stimulation (Fig. 4 *A* and *B*).

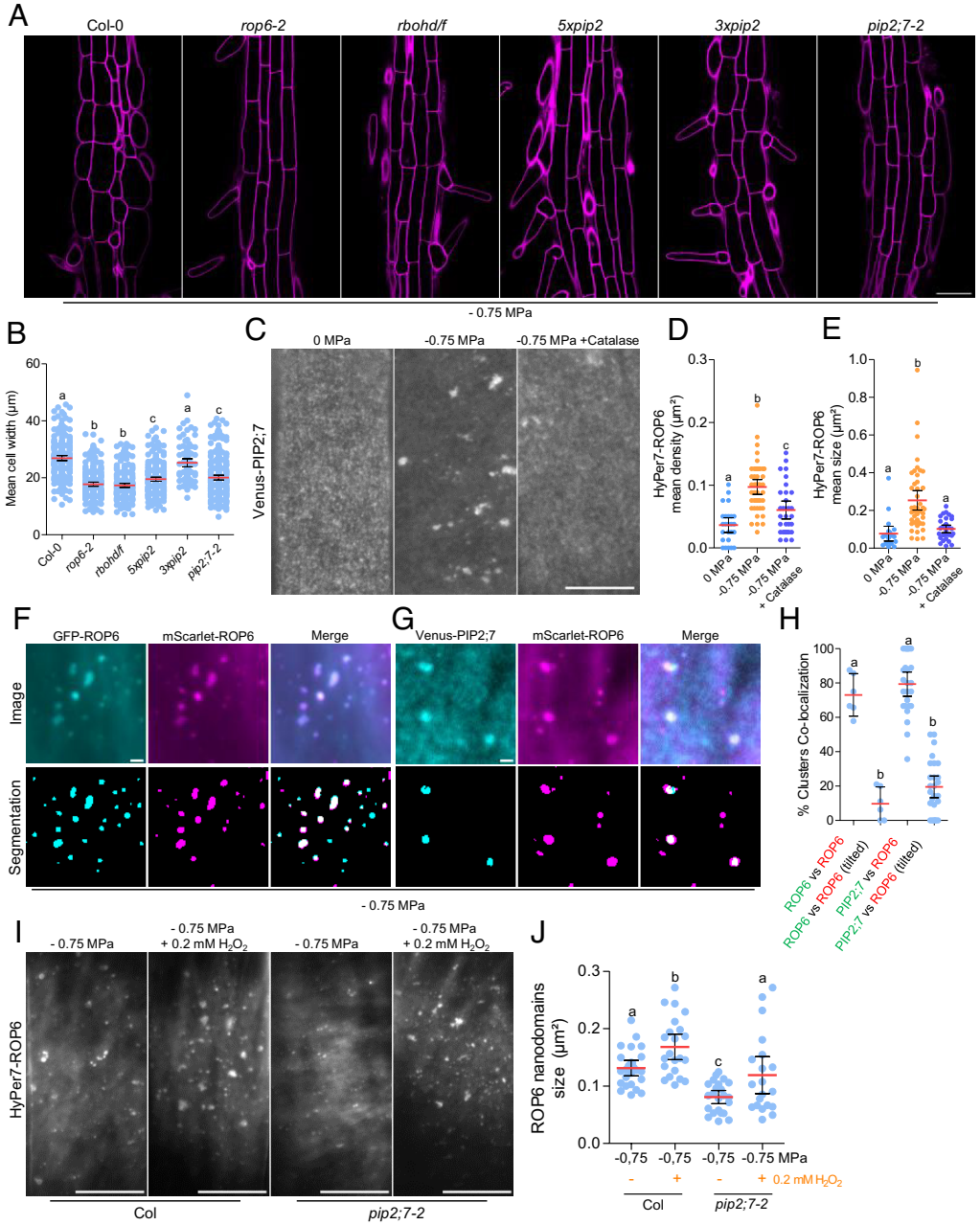

Fig. 4. PIP2;7 colocalizes in osmotically induced ROP6 nanodomains and plays a role in ROP6 clustering. (*A*) Confocal images of root epidermal cells of Col-0, *rop6-2*, *rbohd/f*, *5xpip2*, *3xpip2,* and *pip2-7-2*, transferred for 24 h at −0.75 MPa on vertical petri dishes. Quantification of cell width reflecting the cell swelling is shown in *B*. (*C*) Intensity-based TIRF images of root epidermal cells expressing pPIP2;7:Venus-PIP2;7 in control condition (0 MPa), after osmotic stimulation (15 min, −0.75 MPa) in absence or presence of catalase, with their respective quantification *D* and *E*. (*F–G*) Dual-TIRF images of root epidermal cells expressing p35S:GFP-ROP6 × pPIN2:mScarlet-ROP6 (*F*) or pPIP2;7:mVenus-PIP2;7 × pPIN2:mScarlet-ROP6 (*G*) after osmotic stimulation (15 min, −0.75 MPa). Image segmentation (below panel) was performed to select exclusively pixels among clusters, used to calculate the percentage of colocalization shown in *H*. As a control, 90° tilt was done on one of the two channels. (*I*) TIRF images of root epidermal cells expressing HyPer7-ROP6 (Ex 488) after osmotic stimulation (15 min, −0.75 MPa) cotreated or not with 0.2 mM exogenous H_2O_2 in Col-0 or *pip2;7-2* background, with their respective nanodomain size quantification *J*. Mean with error bars correspond to the 95% CI. For *B*, *D*, *E*, *H*, and *J*, letters show significant differences according to a one-way ANOVA and Tukey's multiple comparisons test at $P < 0.05$. In *B*, n cells >88 from >12 seedlings from two independent replicates. In *D* and *E*, n cells >24 from >4 seedlings from three independent replicates. In *F*, n cells >6 from >4 seedlings from two independent replicates. In J, n cells >20 from >9 seedlings from three independent replicates. For *A*, the scale bar is 50 µm; for *F*, the scale bar is 1 µm; and for *C* and *I*, the scale bar is 10 µm.

PIP2;7 Colocalizes in ROP6-Nanodomains and the Resulting Submembrane Oxidation Reinforcing ROP6 Clustering. Our data suggest a functional link between ROP6 and PIP2;7 in establishing osmotically induced oxidized nanoenvironments. Thus, we investigated Venus–PIP2;7 localization in control conditions or after an osmotic stimulation. Similarly, to ROP6, PIP2;7 forms osmotically induced nanodomains (Fig. 4 *C–E*). Using dual-color TIRF microscopy, we tested whether ROP6 and PIP2;7 nanodomains colocalize. Minutes after osmotic treatment, both mVenus-PIP2;7 and mScarlet-ROP6 formed nanodomains that showed significant colocalization (Fig. 4 *F–H* and *SI Appendix*, Fig. S4*I*). These observations suggest that ROP6 nanodomains, in addition to RBOHD/F, include PIP2;7, likely forming a functional complex that coordinates H_2O_2 production and transport at specific sites of the PM.

Pharmacological and genetic perturbation of H_2O_2 often lead to a change in ROP6 nanodomain shape as observed on TIRF experiments. Specifically, exogenous application of H_2O_2

combined with osmotic stimulation results in the formation of larger ROP6 nanodomains (Fig. 3 *A*, *C*, and *G*). Conversely, reducing apoplastic H_2O_2 -either through catalase treatment or by impairing its transport in the *pip2;7-2* mutant- leads to smaller ROP6 nanodomains (Fig. 3 *A*, *B*, *E*, *G*, and *I*). We then investigated whether the presence of apoplastic H_2O_2 could trigger PIP2;7 nanoclustering, as it does on ROP6. Catalase treatment inhibits the formation of PIP2;7 nanodomains after osmotic signal (Fig. 4 *C*–*E*). These results suggest that ROP6 nanodomain size is either controlled by the presence of PIP2;7 protein (e.g., by direct or indirect protein–protein interaction) or by the local accumulation of cytoplasmic H_2O_2.

To test whether H_2O_2 accumulation is a limiting factor for ROP6 nanodomain size, we treated the *pip2;7-2*xHyPer7-ROP6 line with exogenous H_2O_2, which partially restored the nanodomain size (Fig. 4 *I* and *J*). These results suggest that H_2O_2-enriched nanoenvironments may contribute directly to a feedforward regulatory loop that controls the size of ROP6 nanodomains.

Discussion

The presented work demonstrates that ROP6 is activated by osmotic stress, leading to the formation of ROP6-containing nanodomains at the PM. These nanodomains are associated with discrete oxidized nanoenvironments at the cytosolic side of the PM. Such a process requires diffusion of H_2O_2 across the membrane, in a PIP2;7-aquaporin-dependent manner. In turn, the localized oxidation just below the PM feeds back to regulate the formation of ROP6-containing nanodomains, partially controlling the plant response to osmotic stimulation, as cell isotropic growth. In addition, this model exemplifies that protein clustering in nanodomains could lead to the formation of local gradients of small diffusible molecules like H_2O_2 that is controlled both across and in the plane of the membrane.

Our observations indicate that in addition to the organization of ROP6 and RBOH in nanodomains, aquaporin-dependent H_2O_2 diffusion across the PM also appears to play a critical role. Interestingly, aquaporins, which allow H_2O_2 diffusion, both in heterologous systems and in planta, are regulated by kinases similar to those that modulate RBOH activity. For example, both RBOHF and PIP2;1 are phosphorylated by the kinase OST1/SnRK2.6 (37, 47, 48). The formation of RBOH/PIP nanodomains coregulated by SnRK2 for a coordination between RBOH-dependent ROS production and H_2O_2 diffusion across the membrane regulated by PIPs is an appealing hypothesis, which would need further analyses.

In previous studies, cerium chloride staining combined with electron microscopy was elegantly used to visualize H_2O_2 accumulation in plant cells. For example, cryptogein, a *Phytophthora*-derived elicitor, induces RBOH-dependent H_2O_2 accumulation in discrete foci at the PM when applied to tobacco cells (49). Similar observations were made in the context of lateral root emergence: A discontinuous pattern of H_2O_2 accumulation was observed at the endodermal PM (50). For those two examples, the exact localization of the H_2O_2 accumulation: Facing the cytoplasm or the apoplast remains to be determined. More recently, a highly defined localization of H_2O_2 accumulation in the apoplast was described during the lignification of the Casparian strip (51, 52). These observations suggest that localized H_2O_2 accumulation at the PM extends way beyond the specific context of osmotic stress responses and may occur in diverse cellular processes. Although it remains to be demonstrated if this localized H_2O_2 accumulation results in spatially confined changes in the cytoplasmic redox environment. If yes, this could contribute to the activation of specific downstream signaling cascades mediated by H_2O_2.

Provided protein thiols are sufficiently reactive, H_2O_2 might oxidize target proteins directly. More likely, however, decoding hubs consisting of highly sensitive H_2O_2-sensing proteins capable of transmitting the primary oxidation to protein thiols and the respective downstream targets may exist. In this case, protein–protein interactions and proximity would define the specificity of such oxidation reactions. Detoxification of H_2O_2 in the ascorbate-glutathione pathway has been proposed to trigger changes in the local glutathione redox potential (E_{GSH}), which may cause changes in glutathionylation of target proteins in a reaction catalyzed by glutaredoxins (GRXs) (53). Alternatively, peroxidases acting on H_2O_2 may also function as protein-thiol oxidases as it has recently been shown for the role of cytosolic peroxiredoxin PRXIIB in transmitting the primary oxidation induced by pathogens to the PP2C protein phosphatases ABI1/2 (54). Disulfide formation on ABI1/2 inhibits the phosphatases and ultimately leads to stomatal closure (54). Similarly, it was shown earlier that the glutathione peroxidase Gpx3 (also known as Orp1) in *Saccharomyces cerevisiae* can transmit an H_2O_2 signal to the transcription factor Yap1 to switch it to the active oxidized form (55). The efficiency and specificity of such transmission systems rely on protein proximity, and it can thus be postulated that appropriate scaffold proteins or other structural means exist to mediate proximity between the peroxidase as the H_2O_2 sensor and target proteins. Therefore, we can speculate that localization of GRX, TRX, and potentially GPX in specific nanodomains would determine signal transduction from the membrane. This may account for plant acclimation to osmotic challenges, as osmotically induced ROS have previously been shown to regulate root hydraulic conductivity and the intracellular accumulation of osmolytes such as proline (56, 57).

Recently, in yeast, H_2O_2 concentration changes were carefully mapped, revealing dynamic and highly specific variations in H_2O_2 availability at the level of individual proteins and protein complexes (58). Our data closely mirror this phenomenon, supporting the idea that ROS signaling is spatially discretized within cells. In line with this, we propose that nanodomains composed of RBOHs, ROPs, and PIPs represent a fundamental unit for PM-localized ROS signaling in plants.

Materials and Methods

Plant Material and Growth Condition. *Arabidopsis thaliana* ecotype (Col-0) was used as wild-type control. The following lines were previously published: *pPIP2;7:mVenus-PIP2;7* (44), *p35S:RFP-ROP6* (21), and *pip2;7-2* (42); CRISPR/Cas9-generated deletion leading to a premature stop after 52 amino acids followed by four additional residues RWSH; *SI Appendix*, Fig. S3*D* and Table S1). The multiple *pip* mutant *3xpip2* was obtained by genetic crossing of *pip2;1-2* [SM_3_35928; (59)], *pip2;2-3* [SAIL_169A03; (60)], and *pip2;4-1* (SM_3_20853). The quintuple mutant *5xpip2* was obtained by combining the same insertion lines and *pip2;6-3* [SALK_092140; (61)]. *pip2;7-4* was added by an independent CRISPR/Cas9 approach. The generated deletion leads to a premature stop after 52 amino acids followed by the non-PIP residues WWRS (*SI Appendix*, Fig. S3*D* and Table S1). All insertion lines had been obtained from the *Arabidopsis* stock centers (62). The lines *p35S:HyPer7-ROP6*, *p35S:HyPer7-ROP6-CA*, *5pip2xp35S:HyPer7-ROP6,* and *3pip2xp35S:HyPer7-ROP6* were generated by floral dipping. Crosses *pip2;7-2xp35S:HyPer7-ROP6*, *p35S:RFP-ROP6xpPIN2:mScarlet3-ROP6,* and *pPIP2;7:mVenus-PIP2;7* x *pPIN2:mScarlet3-ROP6* were done in this study. Seeds were surface-sterilized and sow on squared petri dishes containing 50 mL of half-strength Murashige and Skoog medium (MS/2) supplemented with 1% (w/v) sucrose, 2.5 mM MES-KOH (pH 6), and 0.8% agar type E. Seedlings were grown vertically for 5 d under a 16-h light/8-h dark cycle, 70% relative humidity, and a light intensity of 200 $\mu mol \cdot m^{-2} s^{-1}$.

Cloning. HyPer7 clones were generated by Golden Braid (63). In brief, the coding sequence of HyPer7 (30) and ROP6 (At4g35020) was PCR amplified and cloned in pUPD2 vectors. The G15V mutation in ROP6 sequence was introduced by PCR mutagenesis to generate pUPD2-ROP6-CA. Binary vector were made from the assembly of the following parts pUPD2:p35S, pUPD2-HyPer7, pUPD2-ROP6, pUPD2-ROP6-CA, and pUPD2:tNos to create pDGB3a1 *p35s:HyPer7:tNos*, *p35s:HyPer7-ROP6:tNos,* and *p35s:HyPer7-ROP6-CA:tNos*, to generate transcriptional units. To generate pPIN2:mScarlet3-ROP6 a modified GreenGate cloning system was employed (64). Briefly, GreenGate entry vectors were modified by replacing the *caR-ccdB-lacZa* cassette with *lacZa* flanked by SapI restriction sites that overlap with the existing BsaI restriction sites. The shuttle vectors were used in a combined restriction-ligation reaction to clone DNA fragments into the shuttles and create the six modules required for assembly of the binary vector. The following DNA fragments were cloned into their respective shuttle vector: promoter of the *PIN2* gene (module A), mScarlet3 fluorophore [(65); module B], *ROP6* genomic sequence (module C), 3′-UTR of *ROP6* (module D). A combined terminator of the HSP and rbcS E9 terminator sequences was cloned into the classical GreenGate entry vector pGGE000 (module E) (*SI Appendix*, Table S1 for primer sequences). For the binary vector, the backbone of pDGE651 (66) was combined with the orange selection of the GoldenGate vector pAGM4673. All clones were Sanger sequenced. See *SI Appendix*, Fig. S5 for primer sequence.

pip2;7-2 (42) CRISPR was generated using the vector pDGE244 (67) harboring four guide RNA target regions. The binary vector pDGE244 is similar to pDGE146 (67) with Cas9 expressed under control of the PcUBI promoter, a FAST cassette, and a BASTA resistance cassette. The *PIP2;7* reading frame was interrupted after Y52 and the truncated protein prematurely terminated after four additional, non-PIP-encoding amino acids. *pip2;7-4* is an independently CRISPR/Cas9-generated deletion within the *PIP2;7* gene. The vector pDGE250 harbored two guide RNA target regions; here, Cas9 is expressed under the control of AtRPS5a promoter. The nucleotides were eliminated in a region considerably larger than in *pip2;7-2*. Nevertheless, the *PIP2;7* reading frame was interrupted after Y52 and the truncated protein prematurely terminated after four additional, non-PIP-encoding amino acids different from *pip2;7-2*.

Osmotic and Pharmacological Treatments. Osmotic stimulation was applied by first incubating seedlings for 15 min in liquid resting buffer (MS/2, 2.5 mM MES-KOH, pH 6, and 1% w/v sucrose). Seedlings were then transferred to sorbitol buffer composed by the resting buffer supplemented with 150 or 300 mM sorbitol to impose osmotic shocks of −0.26 or −0.75 MPa, respectively. 40 μL/mL catalase was added to both resting (15 min) and sorbitol (15 min) buffers, whereas 0.02 mM, 0.1, 0.2, or 1 mM H_2O_2 was added only for 15 min either to the resting buffer or to resting buffer supplemented with 300 mM sorbitol. Auxin treatments were done for 20 min at 10 μM diluted from a stock at 100 mM raised in DMSO.

HyPer7 Sensor Oxidation Range and Dynamics in a Multiwell Plate Reader. Experiments were performed as described in ref. 68. Briefly, pools of 10-day-old Wild-type or *5xpip2* seedlings expressing either HyPer7-ROP6 or HyPer7-Cyto were placed in independent wells of 96-well plate preloaded with 180 μL of imaging buffer. The redox state of the sensors was followed as the fluorescence ratio between two channels collected sequentially (Channel 1: Ex = 400 ± 5 nm/Em = 520 ± 5 nm; Channel 2: Ex = 482 ± 8 nm/Em = 520 ± 5 nm), using a CLARIOstar plate reader (BMG Labtech, Ortenberg, Germany).

Ratiometric Microscopy. To monitor HyPer7 oxidation dynamics at the root tissue level over time, seedlings were mounted in a perfusion chamber coupled to a ratiometric imaging setup. The setup consisted of a Zeiss Axiovert 200 M microscope equipped with an ORCA-Fusion BT (Hamamatsu) camera, a lambda 10B wheel (Sutter Instrument) and LEDHub (Omicron) illumination source, all controlled via the electronic control unit and software from Inscoper. Images were acquired using a 20×/0.5 objective, with excitation set to 385 nm (370 to 415) or to 470 (430 to 540) and emission collected at 535/30 nm. Sequential images for both channels were acquired every 10 s, and 470/385 ratio images were generated to quantify HyPer7 oxidation.

Prior to treatment, samples were acclimated in resting buffer within the incubation chamber for 30 min to allow the plant to rest and minimize light-induced ROS production. Treatments were applied by complete buffer replacement through three successive perfusions. Washes were performed using the same method.

Image Processing for Ratiometric Microscopy. A custom ImageJ macro was used to process two-channel fluorescence image stacks and compute ratiometric profiles. Each multichannel image was split into separate 405 nm and 488 nm stacks, and background-corrected using a manually defined ROI. Images were converted to 32-bit format, and low-intensity pixels (below 300 for 405 nm and 200 for 488 nm) were set to NaN to exclude background noise. The resulting stacks were saved together with their Z-axis intensity profiles. A ratio image (488/405) was then generated and exported along with its Z-axis profile for quantitative analysis.

Ratiometric Total Internal Reflection Fluorescence Microscopy. A custom TIRF system was configured on an inverted Zeiss microscope equipped with a 100×/1.45 oil-immersion objective. An additional telescope placed in the imaging path provides a final magnification of 150× at the camera sensor. The TIRF angle was manually adjusted to give the best signal to noise ratio. Sequential acquisitions were performed using laser excitation at 488 nm and 405 nm with images collected at 525/25 nm. Image series were collected at three z-planes (0.125 μm step). For each plane, 20 frames per channel were acquired sequentially. To correct for field inhomogeneities, which are inherent to TIRF illumination and vary with wavelength and incidence angle, flat-field correction images with 200 frames per channel were acquired.

Image Processing for Ratiometric TIRF. A custom ImageJ macro was used to batch process multichannel fluorescence images for ratiometric analysis (*SI Appendix*, Fig. S6). Each image file was split into two channels. For each channel, a Z-projection based on average intensity was generated and converted to 32-bit format. To correct for uneven illumination, each projection was divided by the corresponding flat-field correction image. The corrected 488 nm and 405 nm projections were then divided to generate a pixel-by-pixel ratio image (488/405), which was displayed using the "Jet" LUT and a standardized brightness/contrast range (0.6 to 4.0). The resulting ratio images, and the separated 405 nm and 488 nm projection images were then saved in designated output folders.

For quantification of clustering or ratio values, a crop of 100 pixels square was realized on each image. Image segmentation to discriminate pixels among nanodomains was realized using a machine learning–assisted method [with ilastik software, (69)]. Created segmented images were then used to determine ROIs corresponding to pixels among or outside nanodomains.

To determine the distribution of ratio values of the pixels in HyPer7-ROP6 nanodomains, a custom ImageJ macro was used to create a binary mask on segmented images in order to create composite ROI containing all those pixels. An intensity histogram of 41 bins, range 0.8 to 5 (range covering the ratio values observed with HyPer7-ROP6 upon osmotic stimulation) was then generated for each ratio image. The different macros used for image processing are provided in the supplement (*SI Appendix*, Table S2).

In Vitro HyPer7 Characterization. HyPer7 was produced in vitro and purified using His-tag according to Ugalde et al. (30). Purified sensor samples were imaged on the same TIRF setup, using both 488 nm and 405 nm as excitation and 525/25 for emission. To estimate sensor concentration and oxidation state in serial dilution, we use total intensity and 488/405 ratio, respectively. Three different sensor dilutions were imaged to achieve fluorescence signals comparable to those observed inside and outside osmotically induced HyPer7-ROP6 PM nanodomains in living samples.

Lifetime Determination of HyPer7-ROP6 In Planta. Five-day-old *Arabidopsis* seedlings expressing HyPer7-ROP6 treated or not with −0.75 MPa solution were imaged on a Leica Stellaris 8 Falcon confocal microscope coupled with an 80 MHz WLL laser tuned at 488 nm. Images of epidermal cells at the root elongation zone were collected using a 40×/1.1 water immersion objective. The fluorescence was collected between 500 and 550 nm. The fluorescence lifetime of the HyPer7–ROP6 sensor was estimated by phasor plot analysis after wavelet filtering. Pixels with fewer than five detected photons were excluded from the analysis.

Confocal Laser Scanning Microscopy. Localization study of *p35S:HyPer7* (Cyt), *p35S:HyPer7-ROP6*, *pROP6:mCit-ROP6,* and *pPIP2;7:mVenus-PIP2;7* was monitored in five-day-old *Arabidopsis* seedlings stably expressing the respective constructs. Epidermal cells in the root elongation zone were imaged using a 40×1.1 water immersion objective on a Leica SP8 confocal microscope. Excitation was set to 488 nm, and emission was collected at 525/22 nm. Seedlings were grown on

vertical Petri dishes containing standard MS/2 medium as described above and acclimated in liquid resting buffer for 15 min prior to imaging.

Dual Color Total Internal Reflection Fluorescence Microscopy. Dual-color TIRF imaging was performed using the same custom-made TIRF setup described previously. For GFP or mCitrine imaging, excitation was provided by a 488 nm laser (OBIS LX 488-50, Coherent Inc.; 40 mW), and emission was collected using a 525/22 nm filter. For mScarlet imaging, excitation was provided by a 561 nm laser (SAFIR 100 mW), and emission was collected using a 600/20 nm filter. To avoid bleed-through of fluorescence signal between GFP/Venus & mScarlet, single-color plant lines were imaged in each condition, confirming that each fluorophore was detected in well-separated emission channels without detection of any bleed-through signal. Image segmentation was performed as described for Ratiometric TIRF imaging to identify protein clusters and merged to quantify the percentage of colocalizing particles. As a negative control, the red channel was tilted by 90°, the images were remerged, and the resulting percentage of colocalization was determined.

Western Blotting. Root tissue from 12-day-old Col-0, *5xpip2*, *3xpip2,* and *pip2;7-2* plantlets was ground with liquid nitrogen to a fine powder and resuspended in 100 mg/mL of extraction buffer (250 mM Tris-HCl pH6.8, 5% SDS, 40% Glycerol, 0.02% bromophenol blue, and 250 mM DTT). Western blot analysis was performed with antibodies diluted at 1/5,000 for anti-PIP2;1/PIP2;2/PIP2;3 (70) and anti-PIP2;7 (Agrisera AS22 4812) and 1/20,000 for HRP conjugated anti-rabbit in blocking buffer (2% not fat milk, 0.02% Tween 20, and 1× TBS).

Cell Swelling Assay. We performed the cell-swelling assay on 7-day-old *Arabidopsis* plants. 6-day-old grown seedlings (MS/2, 2.5 mM MES-KOH pH5.8, 1% sucrose, and 0.8% Agar Type E) were transferred for 24 h on the same media supplemented with 300 mM Sorbitol. Plants were stained with propidium iodide (1 µL/mL) for 3 min in liquid buffer (MS/2, 2.5 mM MES-KOH pH 5.8, and 1% sucrose) supplemented with 300 mM Sorbitol. After a 2 min wash, the plants were imaged using a confocal microscope.

Statistics. In each experiment, 8 to 10 cells were studied from five to seven different seedlings. All experiments were independently repeated two to three times. Each cell was analyzed individually to include the maximum of the biological variation. Data are expressed as mean ± 95% CI. ANOVA followed by the Tukey test was done, and letters indicate significant differences among means ($P < 0.05$). Statistical analyses such as ANOVA followed by a Tukey post hoc test and *t* test were done in GraphPad Prism.

Data, Materials, and Software Availability. Source data for figures are available at Recherche Data Gouv (https://doi.org/10.57745/8UR5NR) (71). Study data are included in the article and/or *SI Appendix*.

ACKNOWLEDGMENTS. We thank the Montpellier Ressources Imagerie and the Histocytology and Plant Cell Imaging Platform for providing the microscope facility. We acknowledge the MARS imaging facility, member of the national infrastructure France-BioImaging supported by the French National Research Agency (ANR-10-INBS-04). We thank the Root Phenotyping Platform for their support with nondestructive root imaging and kinetic analysis of root system architecture. This work was supported by the Agence National de la Recherche (ANR) through the project CellOsmo (ANR-19-CE20-0008) to AM and joint funding by ANR and the Deutsche Forschungsgemeinschaft (DFG) through the project Nano-ROS (ANR-24-CE92-0024 to A.M. and DFG 545516367 to A.J.M.). Work in Y.J.'s laboratory is supported by the European Research Council under the European Union's Horizon 2020 research and innovation program (Grant Agreement No 101001097-LIPIDEV) to Y.J. and by an EMBO long-term fellowship (ALTF 750-2023) and Marie Curie Sklodowska Action (HORIZON-TMA-MSCA-PF-EF No 101151872-SONA) to P.S. K.J. is grateful for a doctoral fellowship awarded by the German Academic Exchange service (DAAD, Germany).

Author affiliations: [a]Institute for Plant Sciences of Montpellier, Univ Montpellier, CNRS, Institut national de recherche pour l'agriculture, l'alimentation et l'environnement, Institut Agro, Montpellier 34060, France; [b]Institut für Nutzpflanzenwissenschaften und Ressourcenschutz-Chemical Signalling, University of Bonn, Bonn 53117, Germany; [c]Laboratoire Reproduction et Développement des Plantes, Université de Lyon, École normale supérieure de Lyon, Université Claude Bernard Lyon 1, CNRS, Institut national de recherche pour l'agriculture, l'alimentation et l'environnement, Lyon 69342, France; [d]Centre de Biochimie Structurale, CNRS Unité Mixte de Recherche 5048, Institut National de la Santé et de la Recherche Médicale U1054, Université de Montpellier, Montpellier 34090, France; and [e]Department of Environmental Sciences, Institute of Biochemical Plant Pathology, Helmholtz Zentrum München, Neuherberg D-85764, Germany

Author contributions: A.P., M.N., Y.J., L.V., A.J.M., and A.M. designed research; A.P., J.M.U., L.G., A.D., P.S., P.N., J.-B.F., X.D., and K.J. performed research; A.P., P.S., J.-B.F., and M.N. contributed new reagents/analytic tools; A.P., J.M.U., L.G., A.D., P.S., P.N., C.A., J.-B.F., K.J., Y.J., and A.M. analyzed data; and A.P., J.-B.F., M.N., A.S., Y.J., L.V., A.J.M., and A.M. wrote the paper.

1. T. A. Leonard, M. Loose, S. Martens, The membrane surface as a platform that organizes cellular and biochemical processes. *Dev. Cell* **58**, 1315–1332 (2023).
2. I. Levental, E. Lyman, Regulation of membrane protein structure and function by their lipid nano-environment. *Nat. Rev. Mol. Cell Biol.* **24**, 107–122 (2023).
3. Y. Jaillais *et al.*, Guidelines for naming and studying plasma membrane domains in plants. *Nat. Plants* **10**, 1172–1183 (2024).
4. M. A. Torres, J. L. Dangl, J. D. G. Jones, *Arabidopsis* gp91phox homologues AtrbohD and AtrbohF are required for accumulation of reactive oxygen intermediates in the plant defense response. *Proc. Natl. Acad. Sci. U.S.A.* **99**, 517–522 (2002).
5. M. Sagi, R. Fluhr, Production of reactive oxygen species by plant NADPH oxidases. *Plant Physiol.* **141**, 336–340 (2006).
6. M. A. Inupakutika, S. Sengupta, A. R. Devireddy, R. K. Azad, R. Mittler, The evolution of reactive oxygen species metabolism. *J. Exp. Bot.* **67**, 5933–5943 (2016).
7. F. Wu *et al.*, Hydrogen peroxide sensor HPCA1 is an LRR receptor kinase in Arabidopsis. *Nature* **578**, 577–581 (2020).
8. S. Gilroy *et al.*, ROS, calcium, and electric signals: Key mediators of rapid systemic signaling in plants. *Plant Physiol.* **171**, 1606–1615 (2016).
9. Y. Fichman, S. I. Zandalinas, S. Peck, S. Luan, R. Mittler, HPCA1 is required for systemic reactive oxygen species and calcium cell-to-cell signaling and plant acclimation to stress. *Plant Cell* **34**, 4453–4471 (2022).
10. T. Nietzel *et al.*, The fluorescent protein sensor roGFP2-Orp1 monitors in vivo H_2O_2 and thiol redox integration and elucidates intracellular H_2O_2 dynamics during elicitor-induced oxidative burst in Arabidopsis. *New Phytol.* **221**, 1649–1664 (2019).
11. N. Brandes, S. Schmitt, U. Jakob, Thiol-based redox switches in eukaryotic proteins. *Antioxid. Redox Signal.* **11**, 997–1014 (2009).
12. A. J. Meyer *et al.*, Shifting paradigms and novel players in Cys-based redox regulation and ROS signaling in plants–And where to go next. *Biol. Chem.* **402**, 399–423 (2021).
13. R. Mittler, S. I. Zandalinas, Y. Fichman, F. Van Breusegem, Reactive oxygen species signalling in plant stress responses. *Nat. Rev. Mol. Cell Biol.* **23**, 663–679 (2022).
14. R. E. Martin, A. E. Postiglione, G. K. Muday, Reactive oxygen species function as signaling molecules in controlling plant development and hormonal responses. *Curr. Opin. Plant Biol.* **69**, 102293 (2022).
15. G. Feiguelman, Y. Fu, S. Yalovsky, ROP GTPases structure-function and signaling pathways. *Plant Physiol.* **176**, 57–79 (2018).
16. M. Smokvarska, Y. Jaillais, A. Martinière, Function of membrane domains in Rho-of-plant signaling. *Plant Physiol.* **185**, 663–681 (2021).
17. X. Pan, P. Pérez-Henríquez, J. M. Van Norman, Z. Yang, Membrane nanodomains: Dynamic nanobuilding blocks of polarized cell growth. *Plant Physiol.* **193**, 83–97 (2023).
18. H. L. Wong *et al.*, Regulation of rice NADPH oxidase by binding of Rac GTPase to its N-terminal extension. *Plant Cell* **19**, 4022–4034 (2007).
19. K. Kosami *et al.*, The crystal structure of the plant small GTPase OsRac1 reveals its mode of binding to NADPH oxidase. *J. Biol. Chem.* **289**, 28569–28578 (2014).
20. M. Nagano *et al.*, Plasma membrane microdomains are essential for Rac1-RbohB/H-mediated immunity in rice. *Plant Cell* **28**, 1966–1983 (2016).
21. M. Smokvarska *et al.*, A plasma membrane nanodomain ensures signal specificity during osmotic signaling in plants. *Curr. Biol.* **30**, 4654–4664.e4 (2020).
22. M. R. Puli *et al.*, Null mutants of a tomato Rho of plants exhibit enhanced water use efficiency without a penalty to yield. *Proc. Natl. Acad. Sci. U.S.A.* **121**, e2309006120 (2024).
23. J. Park *et al.*, Rac-related GTP-binding protein in elicitor-induced reactive oxygen generation by suspension-cultured soybean cells. *Plant Physiol.* **124**, 725–732 (2000).
24. M. A. Jones *et al.*, The *Arabidopsis* Rop2 GTPase is a positive regulator of both root hair initiation and tip growth. *Plant Cell* **14**, 763–776 (2002).
25. N. Sorek *et al.*, An S-acylation switch of conserved G domain cysteines is required for polarity signaling by ROP GTPases. *Curr. Biol.* **20**, 914–920 (2010).
26. X. Dang *et al.*, Reactive oxygen species mediate conical cell shaping in *Arabidopsis thaliana* petals. *PLoS Genet.* **14**, e1007705 (2018).
27. M. P. Platre *et al.*, Developmental control of plant Rho GTPase nano-organization by the lipid phosphatidylserine. *Science* **364**, 57–62 (2019).
28. M. Smokvarska *et al.*, The receptor kinase FERONIA regulates phosphatidylserine localization at the cell surface to modulate ROP signaling. *Sci. Adv.* **9**, eadd4791 (2023).
29. V. V. Pak *et al.*, Ultrasensitive genetically encoded indicator for hydrogen peroxide identifies roles for the oxidant in cell migration and mitochondrial function. *Cell Metab.* **31**, 642–653.e6 (2020).
30. J. M. Ugalde, M. Schlößer, A. Dongois, A. Martinière, A. J. Meyer, The latest HyPe(r) in plant H_2O_2 biosensing. *Plant Physiol.* **187**, 480–484 (2021).
31. X. Pan *et al.*, Auxin-induced signaling protein nanoclustering contributes to cell polarity formation. *Nat. Commun.* **11**, 3914 (2020).
32. L. Gorgues *et al.*, GEF14 acts as a specific activator of the plant osmotic signaling pathway by controlling ROP6 nanodomain formation. *EMBO Rep.* **26**, 2146–2165 (2025).
33. M. A. Jones, M. J. Raymond, Z. Yang, N. Smirnoff, NADPH oxidase-dependent reactive oxygen species formation required for root hair growth depends on ROP GTPase. *J. Exp. Bot.* **58**, 1261–1270 (2007).
34. C. Waszczak, M. Carmody, J. Kangasjärvi, Reactive oxygen species in plant signaling. *Annu. Rev. Plant Biol.* **69**, 209–236 (2018).

35. H. Chen *et al.*, MSD2, an apoplastic Mn-SOD, contributes to root skotomorphogenic growth by modulating ROS distribution in *Arabidopsis*. *Plant Sci.* **317**, 111192 (2022).
36. C. Hooijmaijers *et al.*, Hydrogen peroxide permeability of plasma membrane aquaporins of *Arabidopsis thaliana*. *J. Plant Res.* **125**, 147–153 (2012).
37. O. Rodrigues *et al.*, Aquaporins facilitate hydrogen peroxide entry into guard cells to mediate XXXXXXXXXXXXXXXXXXXXABA- and pathogen-triggered stomatal closure. *Proc. Natl. Acad. Sci. U.S.A.* **114**, 9200–9205 (2017).
38. D. Israel, S. H. Lee, T. M. Robson, J. J. Zwiazek, Plasma membrane aquaporins of the PIP1 and PIP2 subfamilies facilitate hydrogen peroxide diffusion into plant roots. *BMC Plant Biol.* **22**, 566 (2022).
39. A. R. Schäffner, Aquaporin function, structure, and expression: Are there more surprises to surface in water relations? *Planta* **204**, 131–139 (1998).
40. C. Maurel *et al.*, Aquaporins in plants. *Physiol. Rev.* **95**, 1321–1358 (2015).
41. J.-M. Monneuse *et al.*, Towards the profiling of the *Arabidopsis thaliana* plasma membrane transportome by targeted proteomics. *Proteomics* **11**, 1789–1797 (2011).
42. T. R. Schley *et al.*, The *Arabidopsis* PIP1;1 aquaporin represses lateral root development and nitrate uptake under low nitrate availability. *Plant. Cell. Environ.* **48**, 1500–1513 (2025).
43. J. Chen, S. C. Rogers, M. Kavdia, Analysis of kinetics of Dihydroethidium fluorescence with superoxide using xanthine oxidase and hypoxanthine assay. *Ann. Biomed. Eng.* **41**, 327–337 (2013).
44. C. Hachez *et al.*, *Arabidopsis* SNAREs SYP61 and SYP121 coordinate the trafficking of plasma membrane aquaporin PIP2;7 to modulate the cell membrane water permeability. *Plant Cell* **26**, 3132–3147 (2014).
45. J. Vilarrasa-Blasi *et al.*, Multi-omics analysis of green lineage osmotic stress pathways unveils crucial roles of different cellular compartments. *Nat. Commun.* **15**, 5988 (2024).
46. W. Feng *et al.*, The FERONIA receptor kinase maintains cell-wall integrity during salt stress through Ca^{2+} signaling. *Curr. Biol.* **28**, 666–675.e5 (2018).
47. C. Sirichandra *et al.*, Phosphorylation of the Arabidopsis AtrbohF NADPH oxidase by OST1 protein kinase. *FEBS Lett.* **583**, 2982–2986 (2009).
48. J.-P. Han *et al.*, Fine-tuning of RBOHF activity is achieved by differential phosphorylation and Ca2+ binding. *New Phytol.* **221**, 1935–1949 (2019).
49. J. Lherminier *et al.*, NADPH oxidase-mediated reactive oxygen species production: Subcellular localization and reassessment of its role in plant defense. *Mol. Plant Microbe Interact.* **22**, 868–881 (2009).
50. B. Orman-Ligeza *et al.*, RBOH-mediated ROS production facilitates lateral root emergence in *Arabidopsis*. *Development* **143**, 3328–3339 (2016).
51. Y. Lee, M. C. Rubio, J. Alassimone, N. Geldner, A mechanism for localized lignin deposition in the endodermis. *Cell* **153**, 402–412 (2013).
52. S. Fujita *et al.*, Schengen receptor module drives localized ROS production and lignification in plant roots. *EMBO J.* **39**, e103894 (2020).
53. A. J. Meyer, The integration of glutathione homeostasis and redox signaling. *J. Plant Physiol.* **165**, 1390–1403 (2008).
54. G. Bi *et al.*, The cytosolic thiol peroxidase PRXIIB is an intracellular sensor for H_2O_2 that regulates plant immunity through a redox relay. *Nat. Plants* **8**, 1160–1175 (2022).
55. A. Delaunay, D. Pflieger, M. B. Barrault, J. Vinh, M. B. Toledano, A thiol peroxidase is an H_2O_2 receptor and redox-transducer in gene activation. *Cell* **111**, 471–481 (2002).
56. Y. Boursiac *et al.*, Stimulus-induced downregulation of root water transport involves reactive oxygen species–activated cell signalling and plasma membrane intrinsic protein internalization. *Plant J.* **56**, 207–218 (2008).
57. K. Ben Rejeb *et al.*, Hydrogen peroxide produced by NADPH oxidases increases proline accumulation during salt or mannitol stress in Arabidopsis thaliana. *New Phytol.* **208**, 1138–1148 (2015).
58. P. Kritsiligkou *et al.*, Proteome-wide tagging with an H2O2 biosensor reveals highly localized and dynamic redox microenvironments. *Proc. Natl. Acad. Sci. U.S.A.* **120**, e2314043120 (2023).
59. A. F. Tissier *et al.*, Multiple independent defective suppressor-mutator transposon insertions in *Arabidopsis*: A tool for functional genomics. *Plant Cell* **11**, 1841–1852 (1999).
60. A. Sessions *et al.*, A high-throughput *Arabidopsis* reverse genetics system. *Plant Cell* **14**, 2985–2994 (2002).
61. J. M. Alonso *et al.*, Genome-wide insertional mutagenesis of Arabidopsis thaliana. *Science* **301**, 653–657 (2003).
62. R. L. Scholl, S. T. May, D. H. Ware, Seed and molecular resources for *Arabidopsis*. *Plant Physiol.* **124**, 1477–1480 (2000).
63. A. Sarrion-Perdigones *et al.*, GoldenBraid 2.0: A comprehensive DNA assembly framework for plant synthetic biology. *Plant Physiol.* **162**, 1618–1631 (2013).
64. A. Lampropoulos *et al.*, GreenGate–A novel, versatile, and efficient cloning system for plant transgenesis. *PLoS One* **8**, e83043 (2013).
65. T. W. J. Gadella *et al.*, mScarlet3: A brilliant and fast-maturing red fluorescent protein. *Nat. Methods* **20**, 541–545 (2023).
66. J. Stuttmann *et al.*, Highly efficient multiplex editing: One-shot generation of 8× *Nicotiana benthamiana* and 12× *Arabidopsis* mutants. *Plant J.* **106**, 8–22 (2021).
67. J. Ordon *et al.*, Generation of chromosomal deletions in dicotyledonous plants employing a user-friendly genome editing toolkit. *Plant J.* **89**, 155–168 (2017).
68. J. M. Ugalde, L. Fecker, M. Schwarzländer, S. J. Müller-Schüssele, A. J. Meyer, Live monitoring of ROS-induced cytosolic redox changes with roGFP2-based sensors in plants. *Methods Mol. Biol.* **2526**, 65–85 (2022).
69. S. Berg *et al.*, ilastik: Interactive machine learning for (bio)image analysis. *Nat. Methods* **16**, 1226–1232 (2019), 10.1038/s41592-019-0582-9.
70. O. D. Ines, "Functional analysis of PIP2 aquaporins in Arabidopsis thaliana," Doctoral Dissertation, LMU, Munich, Germany (2008). https://edoc.ub.uni-muenchen.de/12029/1/Da_Ines_Olivier.pdf.
71. A. Poitout *et al.*, Nanoscale regulation of ROS signaling at the plasma membrane tunes the plant response to osmotic stress. Recherche Data Gouv, V1. https://doi.org/10.57745/8UR5NR. Deposited 8 June 2026.